<div style="text-align:center">Chapter 14</div>

Non-Adiabatic Bending Dissociation of OCS Induced by Orbital Unlocking

Toshinori Suzuki[1,2] and Shinkoh Nanbu[2,3]

[1]Institute for Molecular Science, [2]Graduate University for Advanced Studies, and [3]Research Center for Computational Science, Okazaki National Research Institutes, Myodaiji, Okazaki 444–8585, Japan

UV photodissociation of OCS via 2A'($^1\Delta$) leads to a bimodal speed distribution of S($^1D_2$) fragment atoms whereas a single speed distribution characterizes the S atoms emerging from the 1A"($^1\Sigma^-$) surface. The potential energy surfaces of these two states are almost degenerate, meaning that the bimodal state distribution observed for the 2A' state cannot be explained by the topography of the adiabatic surfaces. It is shown that the bimodal distribution originates from concomitant adiabatic and non-adiabatic dissociation processes from the 2A' state. The non-adiabatic transition is due to unlocking of an S atom electron orbital from the C-S axis by rapid rotation of CO.

INTRODUCTION

Within the adiabatic (or Born-Oppenheimer) approximation, a chemical reaction is viewed as the nuclear motion on a single potential energy surface (PES). The nuclear motion over the PES occurs with little or no recrossing in direct reactions, resulting in short trajectories, while long and (pseudo)chaotic trajectories are observed in compound reactions. However, in so far as the nuclear motion occurs on a single PES, these modes of reaction are only different in their complexities. On the other hand, when the energies of different electronic states approach each other at a certain nuclear position, the Born-Oppenheimer approximation becomes totally inaccurate, which is observable by 'non-adiabatic transitions' between the adiabatic PES's (1-4). Their consideration is particularly important when discussing the dynamics of polyatomic molecules, where a number of surface crossing occur between close-lying electronic states. Photodissociation of OCS leads to the same product, CO($^1\Sigma^+$)+S($^1D_2$), from both adiabatic and non-adiabatic dissociation channels. Because of this, the importance of non-adiabatic coupling in OCS was not readily recognized in the past. In this contribution, we describe how the non-adiabatic dissociation dynamics in OCS have been disentangled by two-dimensional photofragment imaging and *ab initio* wavepacket calculations. In the process we will show that one-electron molecular orbital pictures such as Walsh diagrams (5) well illustrate the electronic origin of the non-adiabatic interactions.

TWO-DIMENSIONAL PHOTOFRAGMENT IMAGING

A pump laser pulse dissociates parent molecules to create a rapidly expanding sphere of neutral fragments. In the ion imaging method (6), the neutral fragments are state-selectively ionized by a probe laser pulse and the resulting ion cloud is projected onto an imaging detector that consists of a microchannel plate (MCP) together with a phosphor screen and a CCD (charge-coupled device) camera. When an ion enters one of the channels (10 μm in diameter) in the MCP, secondary electrons are amplified in the channel and accelerated toward the phosphor screen. The electron impact on the phosphor provides a bright light spot that indicates the arrival position of an ion on the MCP. The image on the phosphor screen is captured by the CCD camera and integrated for a number of laser shots. The photofragment velocity components parallel to the detector face (v_x and v_y) are readily determined from the flight time (t) and the arrival position (x, y) of an ion from the relation $v_x=x/t$ and $v_y=y/t$. The ions with different masses are discriminated by the flight times from the ionization region to the detector. Thus, an ion image can be selectively observed for a particular mass of interest by time gating the MCP or the camera. Photofragment imaging uses resonance-enhanced multiphoton ionization (REMPI) to detect the atoms and molecules in a particular quantum state. Therefore, the observed image provides the scattering distribution of state-selected products. It should be noted that electron impact, one-photon, or non-resonant multi-photon ionization methods cannot provide such state-selectivity in ionization. The image obtained is a projection of the 3D fragment velocity distribution onto a 2D detector plane. The

data are numerically inverted to recover the original 3D distribution for quantitative analysis (7). It can be shown mathematically that a cylindrically symmetric 3D object can be reconstructed from a single projection image, if the projection plane involves the symmetry axis. The cylindrical symmetry is ensured for the 3D ion distribution by aligning the pump and probe laser polarization parallel to each other in photodissociation experiment. Therefore, this polarization combination and a projection direction perpendicular to the symmetry axis are usually employed. Inverse Abel transform is most commonly used to invert the 2D projection to the 3D distribution (7).

In our experiment (8), OCS seeded in He or Ar was expanded from a pulsed valve with a stagnation pressure of about 1 bar and collimated by two skimmers. The molecular beam intersects, perpendicularly, the counter-propagated pump and probe laser beams. The time delay between the pump and probe laser pulses is kept less than 20 ns. Both the pump and probe beams are focused with axisymmetric lenses (f = 250 or 300 mm). The photoions produced are accelerated up to a kinetic energy of 4 keV and projected onto the MCP backed by a phosphor screen (36 mm in effective diameter). A high voltage pulse, 1600-1800 V in height and 200 ns in width, is applied to the MCP to time-gate the ions with the particular mass of interest. The transient image on the phosphor screen is captured by a video-rate (CCIR) interline CCD camera and integrated by an image capture board with 16 bit on-board memory. During the integration of an image, the probe laser frequency is scanned over the entire absorption line of the S atom to eliminate Doppler broadening effects due to the fragment recoil velocities.

RESULTS AND DISCUSSION

A. 2D imaging of $S(^1D_2)$ in photodissociation of OCS

OCS is a 16 valence-electron system similar to CO_2, N_2O, and CS_2. The first absorption band of OCS in the UV region is due to transitions to the close-lying $^1\Sigma^-$ and $^1\Delta$ states that arise from the HOMO-LUMO transition. Electric dipole transitions from the ground state $^1\Sigma^+$ to the $^1\Sigma^-$ and $^1\Delta$ states are forbidden. However, bending deformation splits the $^1\Delta$ state into A' and A" and transforms $^1\Sigma^-$ to A" components ($C_{\infty v} \rightarrow C_s$), to which transitions from the ground state are weakly dipole-allowed (9-12).

There are four dissociation channels energetically open for the first absorption band of OCS,

$$OCS \quad \rightarrow CO(^1\Sigma^+) + S(^1D_2) \qquad \Delta H = 98.3 \text{ kcal/mol} \qquad (I)$$

$$\rightarrow CO(^1\Sigma^+) + S(^3P_0) \qquad \Delta H = 73.6 \text{ kcal/mol} \qquad (IIa)$$
$$\rightarrow CO(^1\Sigma^+) + S(^3P_1) \qquad \Delta H = 73.0 \text{ kcal/mol} \qquad (IIb)$$
$$\rightarrow CO(^1\Sigma^+) + S(^3P_2) \qquad \Delta H = 71.9 \text{ kcal/mol} \qquad (IIc).$$

However, the spin-forbidden channels (IIa) - (IIc) contribute only 5% relative to the spin-allowed channel (I) (13). In the following, we focus on the main dissociation channel (I).

Since CO is produced predominantly in the ground vibrational state of $X^1\Sigma^+$ (14), the rotational distribution of CO can be determined from the translational energy distributions of the concomitantly produced S atoms using energy and momentum conservation laws. In fact, observation of the S atoms is advantageous, since it discriminates between the four exit channels unambiguously.

The inverse Abel transforms of the $S(^1D_2)$ images measured at 223, 235, and 248 nm are shown in Fig. 1. The key to assigning the electronic states involved is that dissociation from the A' and A" states leads to S atoms ejected parallel and perpendicular to the pump laser polarization, respectively. Note that the high translational energy component appearing as an outer ring in the ion images varies from an isotropic (223 nm) to anisotropic distribution (248 nm). This means that the high translational-energy component is created from both A' and A", and that the relative photoabsorption cross-section to the A" state increases with respect to A' in the longer wavelength region. Since the only A' state expected in this energy region is the A' Renner-Teller component of the $^1\Delta$ state, the observed photofragments produced parallel to the photolysis laser polarization can be assigned to it. On the other hand, there are two A" states in the region, namely the A" Renner-Teller component of $^1\Delta$ and A"($^1\Sigma^-$). However, from the increasing contribution of A" in the longer wavelength region, the observed perpendicular fragments are assigned to A"($^1\Sigma^-$) that is located at lower energy than the $^1\Delta$ state. The A" Renner-Teller component of $^1\Delta$ exists in higher energy than the A' component.

A striking experimental result is that the speed distribution of S (or the rotational distribution of CO) is bimodal (8,14,15). Since the bending wavefunction of a parent molecule and the rotational distribution of a diatomic fragment can be related by the rotational reflection principle (16), a Gaussian-shaped rotational distribution of CO may be anticipated for a single dissociation channel. The observed bimodal distribution implies that there is bifurcation in dissociation dynamics. The scattering distribution of S atoms observed by ion imaging indicates that the bimodal distribution occurs only for dissociation from the A'($^1\Delta$) state and not for the A"($^1\Sigma^-$) state. The question is why does it occur only from the A'($^1\Delta$) state?
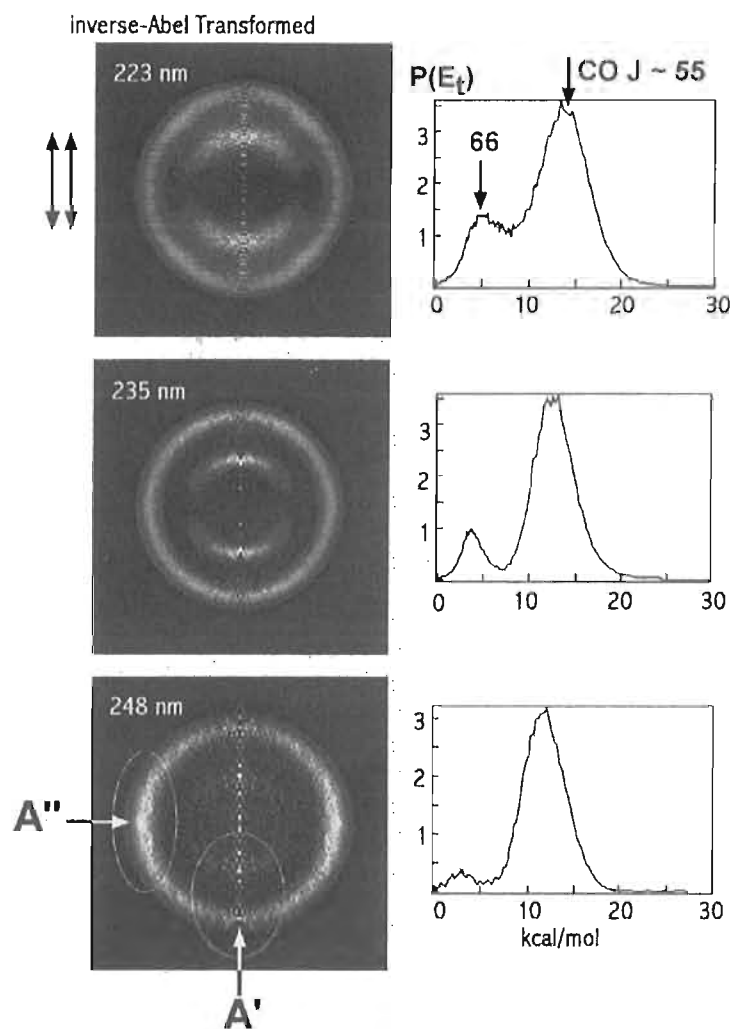
inverse-Abel Transformed

Figure 1 Inverse Abel transforms of the $S(^1D_2)$ images observed for photodissociation at 223, 235, and 248 nm. The center-of-mass translational energy releases calculated from these images are also shown. The fast component gradually changes from an isotropic distribution at 223 nm to an anisotropic distribution at 248 nm. The photoabsorption at 248 nm is dominated by a perpendicular transition to A". A bimodal speed distribution occurs only in dissociation from the A' state.

B. Electronic structure of OCS

To answer this, we calculated the PES's by the *ab initio* MRCI (multi-reference configuration interaction) method (8). In order to describe the low-lying electronic states accurately, the active space was selected as follows:

$$[(9\sigma)(2\pi)(3\pi)(4\pi)(10\sigma)(11\sigma)]^{10}.$$

The CASSCF calculations were performed by considering all possible configurations of the nine active orbitals filled with ten electrons. The restricted closed-shell SCF MO's were used in an initial state-averaged CASSCF calculation for the five A' and three A" states correlating with $S(^3P)+CO$, $S(^1D)+CO$, and $S(^1S)+CO$. The natural orbitals obtained by the CASSCF calculation were used in the final internally-contracted MRCI calculations. The configuration state functions (CSFs) were generated by single and double excitations based on the reference configurations obtained by the CASSCF calculation. However, since the total number of configurations were as large as 6,600,000, only 300,000 configurations were selected in terms of the squares of the CSF coefficients. Since the CO fragment is not vibrationally excited, we fixed the C=O bond length to 1.13 Å and constructed a two-dimensional model with R and θ coordinates. The potential energies and transition dipole moments were calculated at 361 points and spline-interpolated.
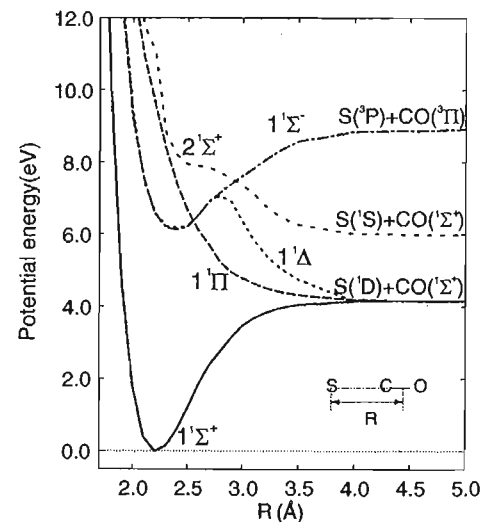

Figure 2 A section of potential energy surfaces for R coordinate in the linear geometry. The CO distance was fixed to 1.13Å. (Adopted with permission from reference 8. Copyright 1998 American Institute of Physics)
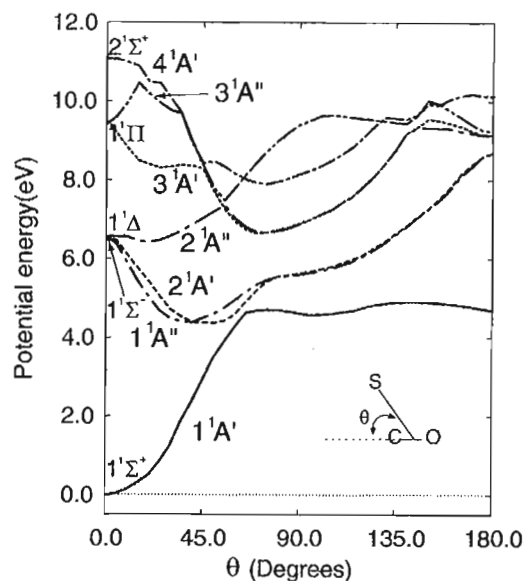
Figure 3 A section of potential energy surfaces for θ coordinate calculated with R=2.2 Å and r=1.13Å. (Adopted with permission from reference 8. Copyright 1998 American Institute of Physics)

Figures 2 and 3 show one-dimensional cuts of the calculated *ab initio* PES's for R and θ. As seen in Fig. 2, both the A'($^1\Delta$) and A"($^1\Sigma^-$) are bound in R, but show conical intersections with the repulsive $^1\Pi$ state at around R=2.5 Å which provide the adiabatic dissociation pathways. It should be noted that both the A'($^1\Delta$) and A"($^1\Sigma^-$) surfaces are steeply declined for θ, as seen in Fig. 3. Therefore, the initial motion on these surfaces is rapid bending of the molecule. Figures 2 and 3 indicate that the topographies of 2A' and 1A" PES's are quite similar.

The bond angles of triatomic molecules can often be qualitatively explained by the diagram of one-electron orbital energies as a function of bending angle known as a Walsh diagram (5). The diagram for CO_2, isovalent with OCS, is shown in Fig. 4. One can clearly see that bending deformation mostly affects the in-plane orbitals. The linearity of CO_2 in the ground state is attributed to destabilization of the HOMO ($4b_2$) by bending. On the other hand, bending deformation significantly stabilizes the LUMO ($6a_1$), so the energies of the HOMO and LUMO are reversed for smaller bond angle. The electronic structure of OCS is essentially the same as that of CO_2. However, the HOMO (12a') and

LUMO (13a') fall in the same symmetry species in the C_s point group so they are symmetry repelled. The out-of-plane HOMO 3a" orbital is not much affected. As a result, 12a' and 3a" have similar orbital energies, and the 2A' and 1A" PES's become almost identical, since these arise predominantly from one electron promotion of 13a'($4\pi_x$)←12a'($3\pi_x$) and 13a'←3a"($3\pi_y$).
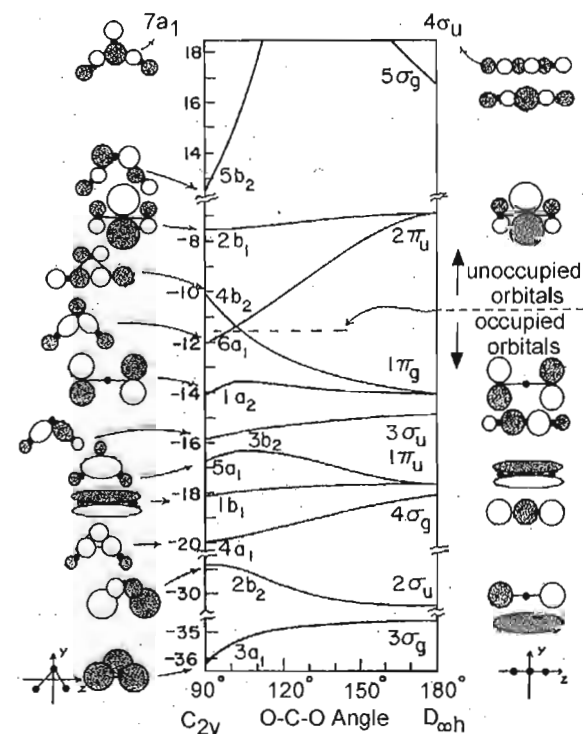

Figure 4 Walsh diagram for CO_2 and schematic MO's adopted with permission from reference 9. The gray color represents the regions of negative phase. Only one member of each pair of the degenerate $1\pi_u$, $1\pi_g$, and $2\pi_u$ orbitals is shown for clarity. The other member of each pair is identical with the one shown, except that it is rotated by 90 degrees about the internuclear axis. For the bond angle of 90 degree, except for the $1b_1$, $1a_2$, and $2b_1$ orbitals, the molecule is shown in the yz plane and all orbitals are in the same plane. For the $1b_1$, $1a_2$, and $2b_1$ orbitals, the molecule is shown in the xz plane and the orbitals are in the same plane (i.e., the orbitals are perpendicular to the molecular plane).

More quantitatively, the orbital energies and shapes of the 13a', 12a', and 3a" MO's were calculated at the CASSCF level with DZP basis set, and these fully supported the qualitative argument described above.

We performed wave packet calculations on the 2A' and 1A" adiabatic *ab initio* surfaces. As is easily understood from the similarity of the 2A' and 1A" PES's and from the rotational reflection principle, dissociation on these two surfaces produce almost identical product distributions, i.e. singly-peaked Gaussians. This is clearly at odds with the observed bimodality in the product distribution and the specificity observed for 2A', suggesting that bimodality cannot be explained by adiabatic dissociation dynamics. Close inspection of Fig. 3 reveals that both the 2A'($^1\Delta$) and 1A"($^1\Sigma^-$) surfaces approach the ground state around $\theta = 65°$, where non-adiabatic transition from 2A' to 1A' might be anticipated.

C. Non-adiabatic transition in the bending coordinate

Non-adiabatic transitions are induced by off-diagonal matrix elements of the nuclear kinetic operator on the electronic wavefunctions. In the case of OCS, a rotational (Coriolis) coupling is essential. If we assume the total angular momentum J to be zero, a rotational coupling term is expressed as follows:

$$H_{rot} = \frac{L^2}{2\mu_R R^2} + \frac{j^2}{2\mu_r r^2} = \left(\frac{1}{2\mu_R R^2} + \frac{1}{2\mu_r r^2} \right) L^2$$

$$= -\left(\frac{1}{2\mu_R R^2} + \frac{1}{2\mu_r r^2} \right) \frac{\partial}{\partial \vartheta} \left(\cot\theta + \frac{\partial}{\partial \vartheta} \right)$$

(1)

where L and j are the orbital angular momentum of relative motion and the rotational angular momentum of a diatomic fragment molecule, respectively. Note that $\frac{1}{2\mu_R R^2}$ diminishes as R increases, while $\frac{1}{2\mu_r r^2}$ due to an internal rotation of CO has no apparent R-dependence, so it becomes relatively more important at large R.

If we take into account only the one-dimensional non-adiabatic coupling element, the non-adiabatic dynamics is reduced to a one-dimensional two-state problem. To solve it, a unitary transformation can be performed on the electronic wavefunctions such that the derivative coupling element $\left\langle \psi_1^e \left| \frac{\partial}{\partial \vartheta} \right| \psi_2^e \right\rangle$ vanishes from the coupled equations for the nuclear motion. In this way, we performed wave packet calculations on the diabatic PES's constructed from the adiabatic *ab initio* PES's (8). The bimodality was well reproduced by our calculations (8).

The experimentally observed non-adiabatic transition efficiency from the 2A' to the 1A' state was 30 % at 223 nm. Such large contribution discovered for this prototypical triatomic molecule illustrates the importance of non-adiabatic transition in polyatomic molecules in general.

On the other hand, the calculated transition efficiency was only 10%. For examining whether this discrepancy is due to the non-adiabatic transition along the R coordinate neglected in the above treatment, we have evaluated it by analytical theory. We decomposed the nuclear position and momentum into the θ and R directions and applied one-dimensional non-adiabatic transition theory at the most critical point of R=2.6 Å and θ=75°. The one-dimensional bending potentials of OCS at R=2.6 Å and those of C-S stretching at θ=75° were extracted from the sections through the 2A' and 1A' PES's. We used the formulas given by Zhu and Nakamura (4) for these two curve-crossing cases to obtain the transition efficiencies. The non-adiabatic transition probabilities calculated for 223 nm photodissociation were 2-3 times larger for the bending (0.09) than the C-S stretching motion (0.03-0.04). Thus, the discrepancy is not reduced by considering the R motion. Full three dimensional analysis on more accurate PES's seems necessary for reproducing the experimental value quantitatively.

D. Non-adiabatic bending dissociation as an orbital unlocking

Fig. 5 shows the picture of MO's along the reaction coordinate with the inertial axis fixed in the same direction. The bending motion is dominated by the fast rotation of CO as we have seen in equation (1). The most critical region for the non-adiabatic transition is between 80 – 120°. An adiabatic process retains an electron in the 13a' orbital that is the p-orbital parallel to the chemical bond, while the non-adiabatic process due to electron deactivation from 13a' to 12a' corresponds to rotation of the p-orbital. In other words, the p-lobe of 13a' on the S atom is pσ in character while that of 12a' is pπ. The non-adiabatic transition of OCS from the 2A' to 1A' state is essentially an unlocking of an electron oribital from the bond axis; that is similar in nature to a pσ-pπ transition observed in atomic collision dynamics.

In Fig. 6, we present the bending potential of 2A' and 1A' around the point of the largest non-adiabatic coupling along the reacton coordinate, R=2.7 Å and θ=65°. It is seen that the separation of the two potentials is much smaller than the one at R=2.2 Å, since the interaction of S with CO is weaker at R=2.7 Å. These are the potentials sampled by the wavepacket in non-adiabatic transition.
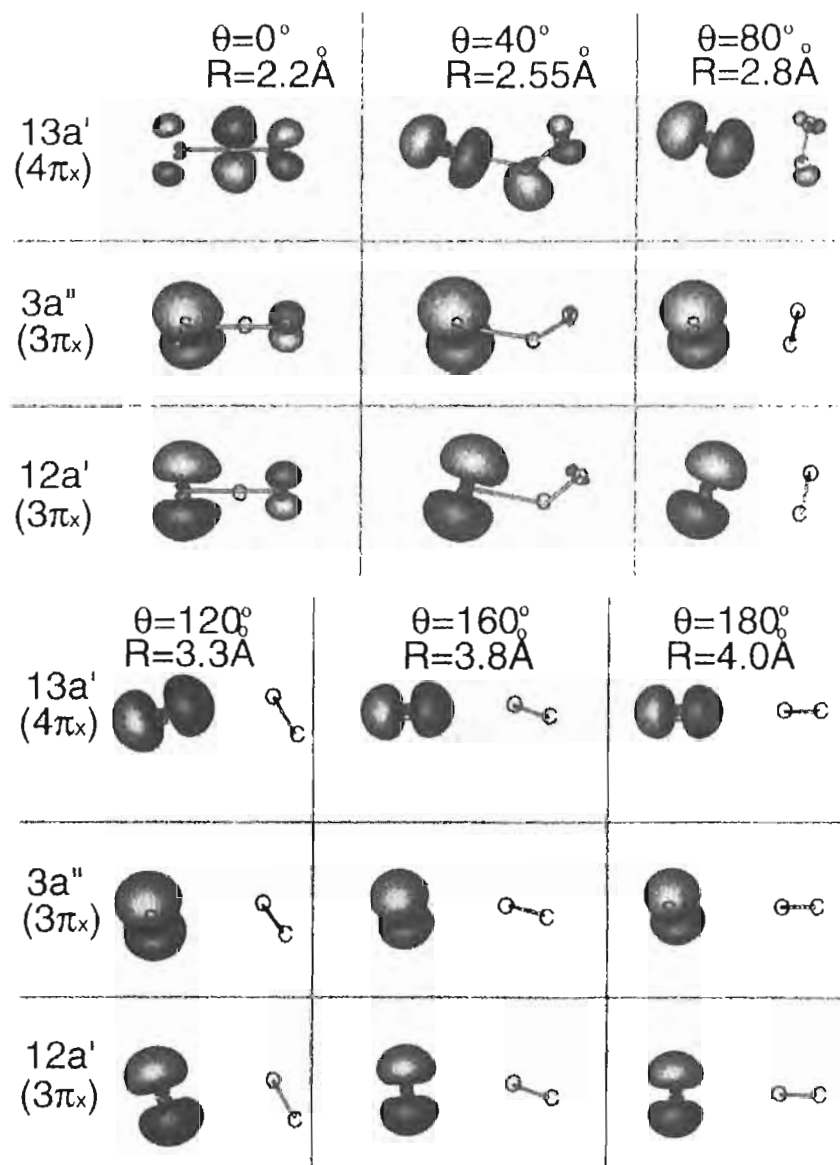
$\theta=0°$
$R=2.2Å$

$\theta=40°$
$R=2.55Å$

$\theta=80°$
$R=2.8Å$

13a'
$(4\pi_x)$

3a"
$(3\pi_x)$

12a'
$(3\pi_x)$

$\theta=120°$
$R=3.3Å$

$\theta=160°$
$R=3.8Å$

$\theta=180°$
$R=4.0Å$

13a'
$(4\pi_x)$

3a"
$(3\pi_x)$

12a'
$(3\pi_x)$

Figure 5 The shape of 13a', 12a', and 3a" molecular orbitals along the reaction coordinate calculated by CASSCF with DZP basis set.
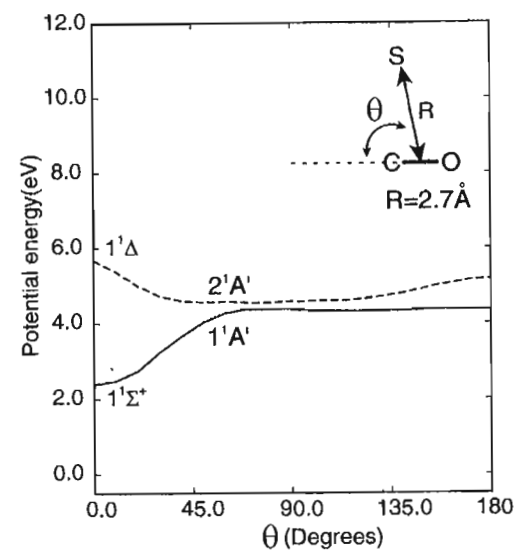
Figure 6 A section of potential energy surface along θ with R=2.7 Å and r=1.13 Å.

$0°$ $40°$ $80°$ $120°$
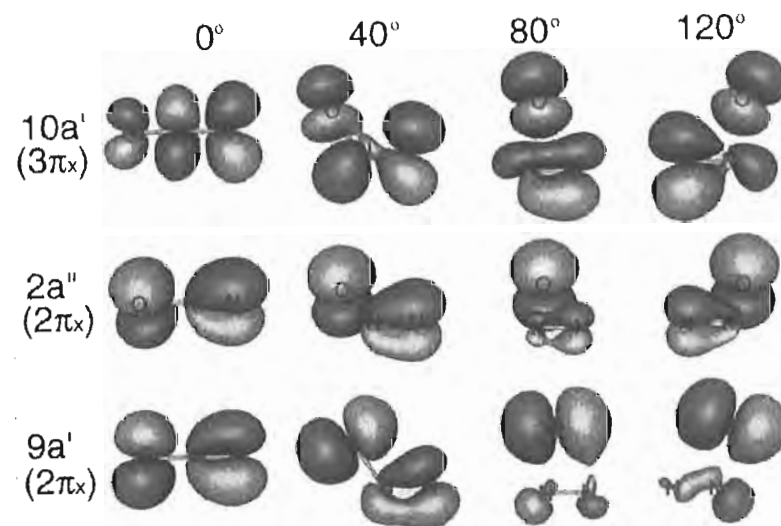
10a'
$(3\pi_x)$

2a"
$(2\pi_x)$

9a'
$(2\pi_x)$

Figure 7 The shapes of HOMO and LUMO of N_2O as a function of θ. R and r were fixed to 1.8 and 1.128, respectively.

As the Walsh diagram predicts, the avoided crossing between the $A'(^1\Delta)$ and $A'(^1\Sigma^+)$ states is not specific for OCS but is general in 16 valence electron systems [5]. In order to demonstrate it, we present the HOMO $9a'(2\pi_x)$ and $2a''(2\pi_y)$ and LUMO $10a'(3\pi_x)$ of the N_2O molecule in Fig. 7. The shapes of the MOs are extremely similar to those of OCS, except for some differences such as the MO amplitude on the central nitrogen atom. As a result, the PES's of N_2O are quite similar to those of OCS [17-19]. In the dissociation of N_2O, however, the light mass of the N atom allows 1.5 times faster motion along R than in OCS. It is quite interesting to compare the dynamics of N_2O molecule with OCS for elucidating the non-adiabatic processes in 16 valence electron systems.

ACKNOWLDGMENT

REFERENCES

1. Landau, L.D.; Lifshitz, E.M. *Quantum Mechanics*; Pergamon Press, Oxford, 1977.
2. Tully, J.C. In *Dynamics of Molecular Collisions;* Miller, W.H.; Plenum, New York, 1976, Part B.
3. Garrett, B.C.; Truhlar, D.G. In *Theoretical Chemistry: Advances and Perspectives*; Henderson, D.; Academic Press, New York, 1981.
4. (a) Nakamura, H., In *Dynamics of Molecules and Chemical Reactions*; Wyatt, R.E.; Zhang, J.Z.H.; Marcell Dekker, New York, 1996.
   (b) Zhu C.; Teranishi Y.; and Nakamura H. In *Advances in Chemical Physics, Volume 117*; Prigogine I. and Rice S.; John Wiley and Sons, 2001.
5. Walsh, A.D. *J. Chem. Soc.* **1953**, 2266.
6. Chandler, D.W.; Houston, P.L. *J. Chem. Phys.* **1987**, *87*, 1445.
7. Whitaker, B.J. In *Research in Chemical Kinetics, Volume I*; Compton, R.G.; Hancock G.; Elsevier, Amsterdam, 1993.
8. Suzuki, T.; Katayanagi, H.; Nanbu, S.; Aoyagi, M. *J. Chem. Phys.* **1998**, *109*, 5778.
9. Rabalais, J.W.; McDonald, J.M.; Scherr, V.; McGlynn, S.P. *Chem. Rev.* **1971**, *71*, 73.
10. Breckenridge, W.H.; Taube, H. *J. Chem. Phys.* **1970**, *52*, 1713.
11. Locker, J.R.; Burkholder, J.B.; Bair, E.J.; Webster, H.A. *J. Phys. Chem.* **1983**, *87*, 1864.
12. Joens, J.A.; Bair, E.J. *J. Phys. Chem.* **1984**, *88*, 6009.
13. Nan, G.; Burak, I.; Houston, P.L. *Chem. Phys. Lett.* **1993**, *209*, 383.
14. Sivakumar, N.; Hall, G.E.; Houston, P.L.; Hepburn, J.W.; Burak, I. *J. Chem. Phys.* **1988**, *88*, 3692.
15. Sato, Y.; Matsumi, Y.; Kawasaki, M.; Tsukiyama, K.; Bersohn, R. *J. Phys. Chem.* **1995**, *99*, 16307.
16. Schinke, R. *Photodissociation Dynamics*, Cambridge University Press, New York, 1993.
17. Hopper, D.G. *J. Chem. Phys.* **1984**, *80*, 4270.
18. Brown, A.; Jimeno, P.; Balint-Kurti, G.G. *J. Phys. Chem. A* **1999**, *103*, 11089.
19. Teule, J.M.; Groenenboom, G.C.; Neyer, D.W.; Chandler, D.W.; Janssen, M.H.M. *Chem. Phys. Lett.* **2000**, *320*, 177.